

Origin of pressure-induced anomalies in the nodal-line ferrimagnet $\text{Mn}_3\text{Si}_2\text{Te}_6$

Varun Venkatasubramanian,¹ Makoto Shimizu,² Daniel Guterding,³ and Harald O. Jeschke¹

¹*Research Institute for Interdisciplinary Science, Okayama University, Okayama 700-8530, Japan*

²*Department of Physics, Graduate School of Science, Kyoto University, Kyoto 606-8502, Japan*

³*Technische Hochschule Brandenburg, Magdeburger Straße 50, 14770 Brandenburg an der Havel, Germany*

A pressure-induced insulator-to-metal transition (IMT) has recently been discovered in the nodal-line ferrimagnet $\text{Mn}_3\text{Si}_2\text{Te}_6$. The electronic phase transition is accompanied by anomalies in the magnetic ordering temperature and the anomalous Hall conductivity, which peak at or near the critical pressure of the IMT. We perform density functional theory (DFT) calculations as a function of pressure to reveal the driving factors behind the IMT and the magnetic anomalies in $\text{Mn}_3\text{Si}_2\text{Te}_6$. We extract Heisenberg Hamiltonians as a function of pressure based on our DFT calculations. Our classical Monte Carlo simulations for these Hamiltonians yield ordering temperatures and magnetic ordering patterns, in agreement with the experimental data. Although we can accurately explain the evolution of magnetism with pressure, it seems that the anomalous Hall conductivity in $\text{Mn}_3\text{Si}_2\text{Te}_6$ cannot be accounted for by intrinsic contributions alone.

I. INTRODUCTION

Magnetic materials with nontrivial band topology have recently emerged as a platform for novel transport phenomena with potential spintronic applications [1–5]. In particular, nodal-line semiconductors and semimetals exhibit a particularly large anomalous Hall effect [6–8] and angular magnetoresistance [9–13].

Among them, $\text{Mn}_3\text{Si}_2\text{Te}_6$ stands out as a ferrimagnetic nodal-line semiconductor that exhibits record-high colossal magnetoresistance (CMR) [14] and angular magnetoresistance (AMR) [12]. These phenomena have been linked to chiral orbital currents [15] and highlight the material as a candidate system where magnetism, topology, and electronic correlations are strongly intertwined.

At ambient pressure, $\text{Mn}_3\text{Si}_2\text{Te}_6$ crystallizes in a trigonal structure (space group $P\bar{3}1c$) [16] and orders ferrimagnetically below $T_C \approx 78$ K [17–19]. Previous studies suggest that its magnetic and electronic properties are closely coupled, with signatures of a field-driven insulator-to-metal transition [20] and current-driven effects on magnetism [21].

Application of pressure reveals even richer physics. At $P = 15.4$ GPa, $\text{Mn}_3\text{Si}_2\text{Te}_6$ undergoes a structural transition to a monoclinic phase, concurrent with an insulator-to-metal transition [22]. From ambient to the critical pressure, the ferrimagnetic ordering temperature increases almost linearly to nearly room temperature, before decreasing again at higher pressures, resulting in a dome-shaped evolution of T_C [22]. After the transition to the monoclinic crystal structure, a pronounced anomalous Hall effect emerges, which peaks near 17 GPa [22]. These correlated anomalies strongly suggest that changes in the electronic structure under compression are intimately linked to the evolution of magnetism.

Here, we investigate the microscopic origin of these pressure-induced anomalies. Using density functional theory (DFT) calculations combined with classical Monte Carlo simulations, we extract exchange couplings, ordering temperatures and anisotropies across the structural

transition, as well as the intrinsic anomalous Hall conductivity. Our results provide a comprehensive picture of how pressure tunes the interplay between electronic and magnetic degrees of freedom in $\text{Mn}_3\text{Si}_2\text{Te}_6$.

II. RESULTS

For pressures up to $P = 15.4$ GPa in the trigonal space group $P\bar{3}1c$, the crystal structures are obtained by DFT structure relaxation, using a GGA+ U functional for a proper description of strong electronic interactions of the $3d$ electrons of the Mn^{2+} ions. We fix the value of the Hund’s rule coupling at $J_H = 0.76$ eV [23]. The relaxed structural parameters are not strongly dependent on the precise value of the on-site interaction U ; for this reason, we use a generic value of $U = 5$ eV which has successfully described the magnetism of other Mn based magnets [24]. For the crystal structures, we use the lattice parameters determined experimentally in Ref. 22. We interpolate the lattice parameters in order to obtain a regular and dense mesh of pressures values.

For the trigonal structures, we obtain the internal positions by DFT+ U structure relaxation in the ferrimagnetic state that is known to be the ground state. Note, however, that while the structures differ significantly between relaxation in non-magnetic and magnetic states, the magnetic order (ferromagnetic or ferrimagnetic) does not play a significant role. More details on the structures are given in the Supplementary Materials [25].

Preparation of the monoclinic high pressure structures is more involved. We again interpolate the lattice parameters of the candidate $C2c$ structures between $P = 15.4$ GPa and 25 GPa that were experimentally determined to be the best candidate for the high pressure space group [22]. However, we found that DFT relaxation of internal parameters took the structure too far away from the single fully determined crystal structure at $P = 22.3$ GPa. This happens independent of the exchange correlation functional and is comparable to the situation in CrGeTe_3 , where we similarly found that the

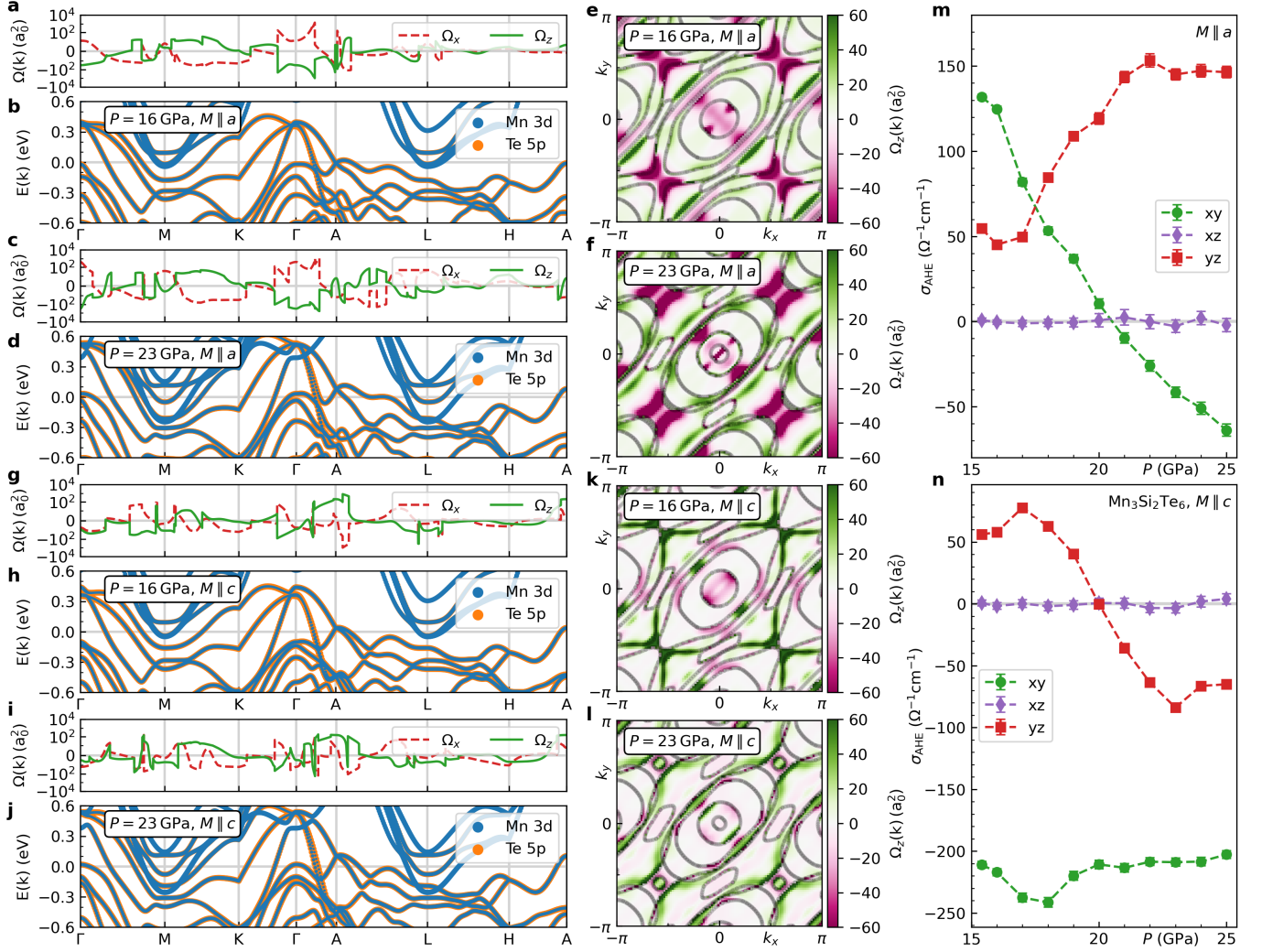


FIG. 1. Electronic structure, total Berry curvature and anomalous Hall conductivity of $\text{Mn}_3\text{Si}_2\text{Te}_6$ in the ferrimagnetic ground state as a function of pressure and spin quantization axis. (a,c) show the total Berry curvature Ω_x and Ω_z (in units of squared Bohr radii a_0^2) and (b,d) show the electronic band structure with orbital weights on a high-symmetry path through the Brillouin zone for spin quantization axis parallel to the a direction at a pressure of 16 and 23 GPa, respectively. (e) and (f) show cuts of the total Berry curvature Ω_z in the k_x - k_y plane at $k_z = 0$ for the same pressures and the same orientation of spin quantization axis. The colour scale is cut off at a value of ± 60 . The grey shaded area represents the Fermi surface. (g-l) show the electronic structure and total Berry curvature for spin quantization axis parallel to the c direction and all other parameters equal to (a-f). (m) and (n) show the intrinsic contribution to the anomalous Hall conductivity in the xy , xz and yz planes as a function of pressure calculated from relativistic DFT calculations in the ferrimagnetic state with spin quantization axis parallel to the a direction (easy axis) and the c direction (hard axis), respectively.

experimental crystal structure cannot be precisely reproduced by any DFT functional [26]. For this reason, we keep the internal structure parameters constant at the values determined experimentally for $P = 22.3$ GPa.

In fact, the crystal structure of $\text{Mn}_3\text{Si}_2\text{Te}_6$ is similar to van der Waals chalcogenides: layers of MnSiTe_3 are self-intercalated with Mn atoms, leading to alternating honeycomb and triangular Mn layers [16, 22]. At the critical pressure of $P = 15.4$ GPa, the monoclinic phase transition splits the tellurium positions into three inequivalent sites and the MnSiTe_3 layers slide slightly with respect to each other [22].

Our DFT calculations with ferrimagnetic spin configuration reproduce the experimentally observed IMT of $\text{Mn}_3\text{Si}_2\text{Te}_6$ at a pressure of $P = 15.4$ GPa. For lower pressures, the system is a band insulator. For higher pressures, the system becomes metallic. The Berry curvature in the metallic phase shows a complex momentum structure with positive and negative contributions of high absolute value (see Fig. 1). In the metallic phase, both the electronic band structure and these momentum-space structures of the Berry curvature evolve gradually as a function of pressure.

The anomalous Hall conductivity (AHC) arises from

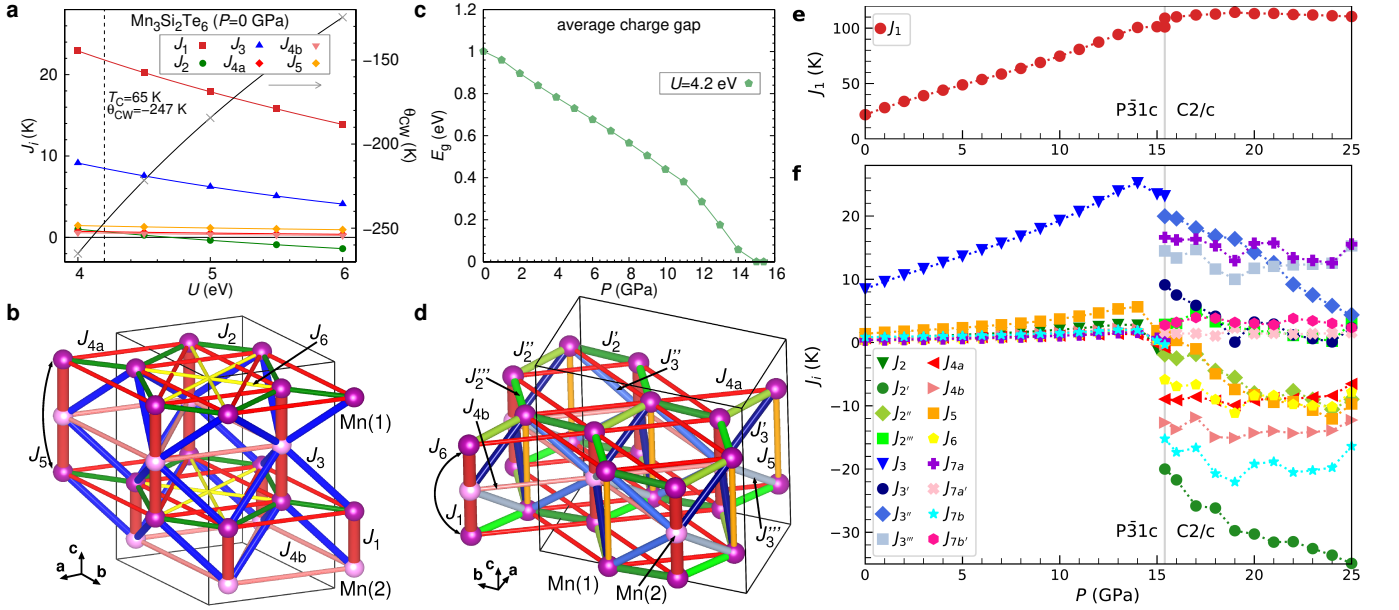


FIG. 2. (a) DFT energy mapping for $\text{Mn}_3\text{Si}_2\text{Te}_6$ at ambient pressure as a function of the on-site Coulomb repulsion U . The dashed line denotes the value of on-site Coulomb repulsion $U = 4.2 \text{ eV}$, which we choose for the remainder of our study. For this interaction strength, we obtain $\Theta_{\text{CW}} = -247 \text{ K}$ as the mean-field Curie-Weiss temperature and $T_{\text{C}} = 65 \text{ K}$ as the ordering temperature in classical Monte Carlo, which both agree well with experimental values. (b) Relevant exchange paths in $\text{Mn}_3\text{Si}_2\text{Te}_6$, shown for the high symmetry, trigonal $P\bar{3}1c$ space group. (c) Average charge gap of all magnetic configurations included in the DFT energy mapping as a function of pressure. (d) Relevant exchange paths in $\text{Mn}_3\text{Si}_2\text{Te}_6$, shown for the low symmetry, monoclinic $C2/c$ space group. (e) Antiferromagnetic intra-trimer (nearest neighbour) exchange coupling J_1 as a function of pressure. (f) Next-nearest neighbour and longer range exchange couplings J_{ij} as a function of pressure. The interaction parameters are $U = 4.2 \text{ eV}$ and $J_{\text{H}} = 0.76 \text{ eV}$.

the Berry curvature as the integral over large positive and negative contributions, i.e. we can expect the AHC to be very sensitive to details of the electronic structure. Although changes in the AHC as a function of pressure are gradual, we observe sign changes in some components of the conductivity tensor, while others are relatively stable. The xz component is zero within numerical accuracy, regardless of the choice of quantization axis (which corresponds to the direction of an applied magnetic field in experiment). The xy and yz components show qualitative changes when the spin quantization axis is rotated from the easy axis (along a) to the hard axis (along c). Normally, the AHC is measured in large magnetic field. Therefore, which orientation of the spin quantization axis in DFT is appropriate for comparison to experiment depends on the spin-flop field of $\text{Mn}_3\text{Si}_2\text{Te}_6$, which we determine together with other magnetic properties of this material.

Next, we establish the Heisenberg Hamiltonian parameters for $\text{Mn}_3\text{Si}_2\text{Te}_6$ as a function of pressure. We base our calculations on experimental crystal structures as described above. In order to determine the exchange interactions, we now apply the DFT energy mapping technique. This involves DFT calculations for a large number of spin configurations in low symmetry structures of $\text{Mn}_3\text{Si}_2\text{Te}_6$ and fitting the total energies with the Heisen-

berg Hamiltonian

$$H = \sum_{i < j} J_{ij} \mathbf{S}_i \cdot \mathbf{S}_j, \quad (1)$$

where \mathbf{S}_i are spin operators, and we do not double count bonds. This approach regularly yields excellent results in magnetic insulators [27, 28] but it has also been useful for understanding the magnetism in semiconducting and metallic CrGeTe_3 under pressure [26, 29]. In fact, the latter material shares many similarities with $\text{Mn}_3\text{Si}_2\text{Te}_6$, for example the structural elements of the Ge_2Te_6 or Si_2Te_6 units and the observation of an anomalous Hall effect under pressure [22, 30].

In the DFT energy mapping approach, there are two parameters that affect the overall energy scale of the exchange couplings, the on-site interaction U and the Hund's rule coupling J_{H} . The latter is expected to have little material dependence, and we fix it to $J_{\text{H}} = 0.76 \text{ eV}$ as suggested in Ref. [23]. For the on-site Coulomb interaction U , we exploit experimental observations at ambient pressure and then fix U , assuming that it is not strongly pressure dependent. The experimental Curie-Weiss temperature $T_{\text{CW}} = -277 \text{ K}$ and the ferrimagnetic ordering temperature $T_{\text{C}} = 78 \text{ K}$ at ambient pressure [17] are well reproduced in our theoretical calculations if we choose $U = 4.2 \text{ eV}$ for this entire study. With the fixed parameters $U = 4.2 \text{ eV}$ and $J_{\text{H}} = 0.76 \text{ eV}$, we now cal-

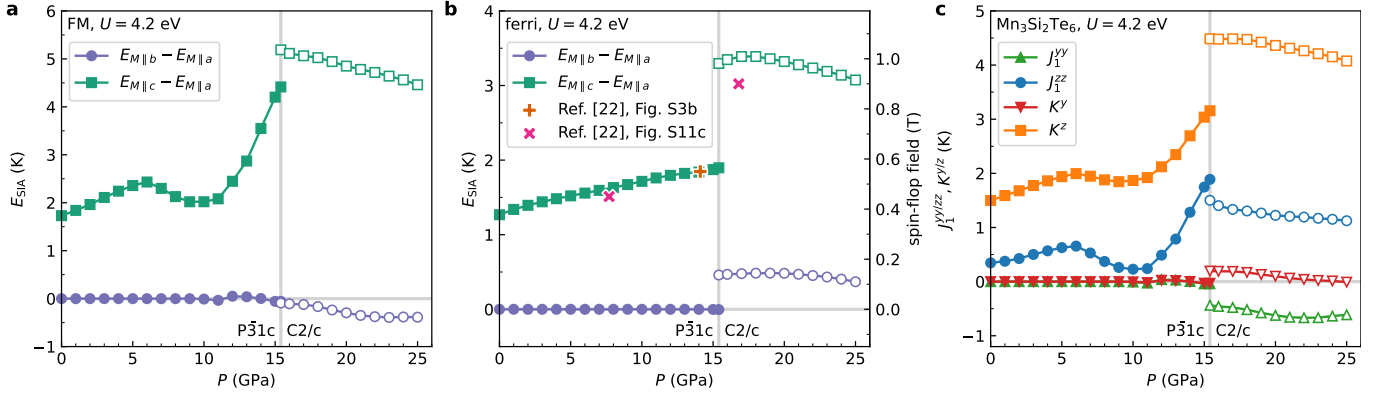


FIG. 3. Single-ion and nearest-neighbour exchange anisotropies of $\text{Mn}_3\text{Si}_2\text{Te}_6$ from the DFT energy mapping as a function of pressure with $U = 4.2$ eV. Labels $C2/c$ and $P31c$ denote the crystal symmetries on both sides of the phase transition. (a) shows the raw energy differences per Mn atom (also divided by the square of the spin $S = 5/2$) for the ferromagnetic state as a function of the spin quantization axis. (b) shows the raw energy differences per Mn atom (also divided by the square of the spin $S = 5/2$) for the ferrimagnetic ground state and compares these energy differences to the spin-flop fields from Ref. [22] at the few experimentally known pressures. (c) shows the anisotropic single-ion (K^y and K^z) and nearest-neighbour exchange (J_1^{yy} and J_1^{zz}) parameters as a function of pressure determined from raw energy differences.

culate the Heisenberg Hamiltonian parameters; they are summarized in Fig. 2.

We find that in the trigonal low pressure region, Hamiltonians are dominated by antiferromagnetic J_1 and J_3 . J_1 mediates the exchange between two Mn1 and one Mn2 in the nearest-neighbour Mn trimer; in this sense, the network defined by J_1 is zero-dimensional, and below the ordering temperature for J_1 , the trimers order in up-down-up states and the effective moment of the system is reduced to one third. J_3 defines a honeycomb network in the ab plane. It also connects Mn1 and Mn2 sites, and therefore the Neel state formed by unfrustrated J_3 corresponds to a ferromagnetic order of the trimers with effective spin of $S_{\text{eff}} = \frac{5}{2}$. Therefore, the nearly linear increase of J_3 in the insulating phase up to $P = 15.4$ GPa indicates that we can expect a similar linear increase for the ferrimagnetic ordering temperature of the material.

We confirm this expectation by classical Monte Carlo (cMC) simulation of the full Hamiltonians shown in Fig. 2. In Fig. 4 we show that the calculated T_C from our Hamiltonians can explain the T_C increase seen in experimental resistivity and susceptibility data from Ref. 22 very well. In our calculations, the pressure induced insulator to metal transition occurs between 14 and 16 GPa (see Fig. 2(c)). Between these two pressures, we observe a clear change in the pressure evolution of the exchange interactions: J_1 levels off, and most of the subleading couplings begin to drop or even to turn negative (ferromagnetic). The phase transition from trigonal to monoclinic space group leads to significant changes in the exchange couplings.

The dominant coupling J_1 that is responsible for the $S = 5/2$ trimers remains constant at around 100 K up to the highest pressure $P = 25$ GPa. The second neighbour coupling J_2 , which defines a honeycomb network for Mn1, splits into three distinct couplings; while J_2 was

near zero in the trigonal structure, possibly due to a compensation between ferromagnetic and antiferromagnetic contributions to the exchange, the three couplings J'_2 , J''_2 and J'''_2 in the monoclinic structure take on substantial ferromagnetic values. The coupling J_3 , which defines a buckled honeycomb network connecting Mn1 and Mn2, also splits into three couplings at the transition to monoclinic symmetry. They remain mostly antiferromagnetic but are significantly smaller than J_3 before the transition. The average of J'_3 , J''_3 and J'''_3 shows an almost linear decrease. The coupling J_{4a} connects second nearest neighbours in the Mn1 honeycomb network while J_{4b} form a Mn2 triangular lattice. Both are small in $P31c$ but become significant and ferromagnetic in $C2c$. The coupling J_5 is the second nearest neighbour in the Mn trimer at twice the length of J_1 . Small and antiferromagnetic in trigonal symmetry (slightly destabilizing the up-down-up order in the trimer), it becomes increasingly ferromagnetic in monoclinic symmetry where it stabilizes the up-down-up trimer order.

To determine the anisotropies from DFT, we calculate the total energy in ferri- and ferromagnetic spin configuration as a function of the spin quantization axis. We then perform an additional energy mapping, considering that the isotropic part of the Hamiltonian H_{iso} (Eq. 1) is independent of the quantization axis. This allows us to resolve the anisotropy terms in

$$H = H_{\text{iso}} + \sum_{i < j} (J_{ij}^{yy} S_i^y S_j^y + J_{ij}^{zz} S_i^z S_j^z) + \sum_i (K^y (S_i^y)^2 + K^z (S_i^z)^2), \quad (2)$$

where J_{ij}^{yy} and J_{ij}^{zz} are nearest neighbour exchange anisotropies and K_i^y and K_i^z are single-ion anisotropies. In the trigonal phase we have $J_{ij}^{yy} = 0$ and $K_i^y = 0$ due

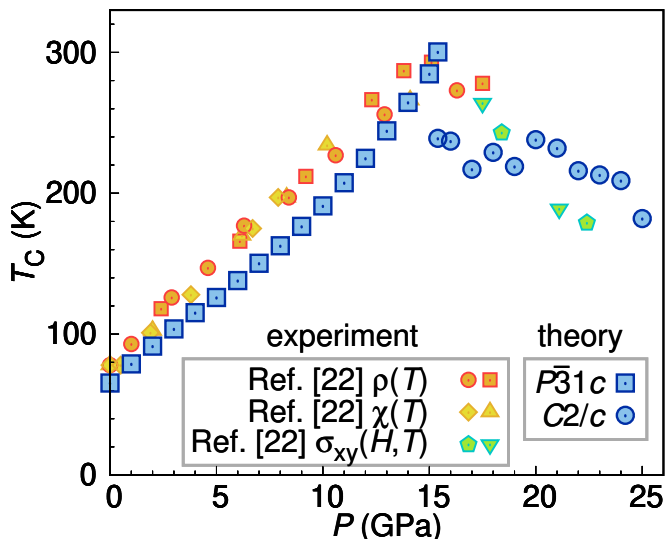


FIG. 4. Predicted ferrimagnetic ordering temperatures (blue symbols) for $\text{Mn}_3\text{Si}_2\text{Te}_6$ as function of pressure, compared to the experimental data from Ref. [22] (yellow, orange and green symbols). The theoretical prediction is based on the isotropic Hamiltonian determined from the DFT energy mapping, which we use to simulate magnetic configurations in classical Monte Carlo.

to the crystal symmetry.

The DFT energies, evaluated as a function of pressure, magnetic ordering pattern (FM or ferrimagnetic), and spin quantization axis (see Fig. 3(a,b)), clearly indicate that ferrimagnetic ordering is more stable than FM, and that the ab plane constitutes the easy plane in trigonal $\text{Mn}_3\text{Si}_2\text{Te}_6$. In the monoclinic phase, the energies of the a and b directions split (see Fig. 3(b)). Alignment parallel to the b axis yields an energy slightly above the a axis. The energy distance with respect to the c axis increases. The ferromagnetic state, which is much higher in energy than the ferrimagnetic state, shows a similar trend (see Fig. 3(a)), although the b axis is slightly lower in energy than the a axis.

The anisotropy energies can be converted into a magnetic field, which is necessary to rotate spins from the easy plane or axis to the hard axis. For this we need to consider the rotation angle between crystal axes, which differs from 90° in the monoclinic phase. These estimates agree very well with the observed spin-flop fields in Ref. [22] (see right axis in Fig. 3(b)).

As expected from the energies, in the trigonal phase we find positive exchange and single-ion anisotropies for the z direction, while the anisotropies for the y direction are basically zero, except for small convergence errors in the DFT energies (see Fig. 3(c)). Since nearest neighbour spins in the ferrimagnetic trimer of the ground state are antiparallel, the energy difference between ab plane and c axis is mostly due to the single-ion anisotropy K^z , while the exchange anisotropy J^{zz} actually decreases the anisotropy energy.

In the monoclinic phase, the parameters associated with the c axis change only quantitatively compared to the trigonal phase: the exchange anisotropy J^{zz} remains almost constant, while the single-ion anisotropy K^z increases slightly (see Fig. 3(c)). The parameters associated with the b axis become non-zero: while the positive single-ion anisotropy K^y is quite small, the anisotropy energy for the b axis is generated mostly by the negative exchange anisotropy J^{yy} .

III. DISCUSSION

Our results for the electronic structure of $\text{Mn}_3\text{Si}_2\text{Te}_6$ reproduce the experimentally observed IMT at the structural phase transition. Interestingly, the average charge gap of the magnetic configurations in our study decreases smoothly as a function of pressure and finally vanishes at the structural phase transition (see Fig. 2(c)). This result seems to agree with the smooth decrease of longitudinal resistivity as a function of pressure observed in experiment [22].

Although our calculations faithfully describe the experimentally known electronic and magnetic properties of $\text{Mn}_3\text{Si}_2\text{Te}_6$ on both sides of the structural phase transition, we cannot fully explain the experimentally observed dome in the anomalous Hall conductivity as a function of pressure (see Fig. 1) upon entering the monoclinic metallic phase [22]. A similar qualitative mismatch has been observed for the closely related van der Waals ferromagnet CrGeTe_3 , where discrepancies have been attributed to extrinsic effects [30–32].

Since the AHE is measured in large magnetic field far above the spin-flop field of ~ 1 T (see Fig. 3(b)), we can assume the spins to be oriented along the hard axis (c axis). Therefore, the experimental AHC should be compared to Fig. 1(n). DFT predicts a large intrinsic contribution with negative sign to the xy component of the AHC, while experiment shows small positive values, which decrease between about 16 and 21 GPa [22]. Based on our findings in Fig. 1(n) it seems possible that the experimentally observed behaviour could be the result of partial cancellation between the large negative intrinsic contribution and a (hypothetical) positive extrinsic contribution of about the same size. This issue merits further investigation.

Our results for the isotropic exchange couplings of $\text{Mn}_3\text{Si}_2\text{Te}_6$ show a rather simple picture of unfrustrated antiferromagnetic exchange in the trigonal high-symmetry structure. In the metallic monoclinic low-symmetry structure, many exchange paths contribute with opposite signs (see Fig. 2(f)), which potentially leads to cancellation of contributions and a destabilization of the ferrimagnetic ground state as well as a lower ordering temperature. In this sense, the decreasing ordering temperature (see Fig. 4) cannot be attributed to the decrease or increase of a single exchange coupling. It is rather the product of qualitatively different exchange

Hamiltonians in the trigonal vs. monoclinic structures. Nevertheless, our classical Monte Carlo simulations for the ordering temperature (see Fig. 4) and the ground state faithfully reproduce the experimentally observed behaviour, also in the low-symmetry phase whose structure is not yet resolved with absolute certainty. This indicates that the $C2/c$ structure is a good candidate for the low-symmetry phase, where the complex cancellation of ferromagnetic and antiferromagnetic exchange paths seems to be the root cause of the decreased ordering temperature.

Our estimates of the exchange and single-ion anisotropies agree with the experimental observations. $\text{Mn}_3\text{Si}_2\text{Te}_6$ in the low-pressure high-symmetry phase has an easy plane in the ab plane and a hard axis in the c direction (see Fig. 3(b)). In the monoclinic phase, the a and b directions split. The a direction becomes the easy axis, while the b direction is only slightly higher in energy. The c direction remains the hard axis. The behaviour of individual anisotropy parameters is rather complex and non-monotonic as a function of pressure (see Fig. 3(c)). Nevertheless, the resulting spin-flop fields (see Fig. 3(b)) quantitatively agree with experimental data from Ref. [22]. With a spin-flop field of ~ 1 T and the strong effect of the orientation of the spin quantization axis on electronic structure, anomalous Hall effect and magnetic properties, comparisons between experiment and theory need to carefully consider the size of magnetic field applied in experiment and its implications for the spin quantization axis in DFT.

In summary, our description of the electronic structure of $\text{Mn}_3\text{Si}_2\text{Te}_6$ is in good agreement with experimental data. The remaining discrepancies for the AHE can probably be explained by cancellation of intrinsic and extrinsic effects. The complex magnetic Hamiltonian for $\text{Mn}_3\text{Si}_2\text{Te}_6$ including isotropic and anisotropic terms faithfully reproduces the magnetic properties of this material as a function of pressure.

IV. METHODS

A. Density functional theory-based energy mapping

We perform density functional theory (DFT) calculations within the full potential local orbital (FPLO) method [33] and using the generalized gradient approximation (GGA) [34] for the exchange-correlation functional. We account for the strong interactions on Mn^{2+} ions using a DFT+ U correction [35]. The experimental crystal structures under pressure were imported from Ref. [22] and interpolated smoothly using splines.

The DFT-based energy mapping approach requires accurate DFT energies for a large set of distinct spin configurations, which are then used to fit the exchange parameters between the spin-5/2 manganese atoms in Eq. 1 by matching the classical energies of the Heisenberg Hamil-

tonian with the calculated DFT energies. In the trigonal $P31c$ space group, we use $2 \times 1 \times 1$ supercells with 12 distinct Mn^{2+} ions. Calculating 30 spin configurations, we can resolve 14 exchange interactions up to a distance of about three times the nearest neighbour Mn-Mn distance. In the monoclinic $C2c$ space group, we ensure low statistical error bars on the exchange interactions by calculating 100 spin configurations in order to resolve 16 exchange couplings.

Single-ion and exchange anisotropies were extracted from DFT by rotating the spin quantization axis and calculating total energies in both ferri- and ferromagnetic spin configuration. Using six DFT energies (from the two spin configurations multiplied by the three choices for the spin quantization axis), we can solve the corresponding system of linear equations for the anisotropies.

In the trigonal phase, we know that the a and b directions are equivalent. Therefore, we have $J_1^{yy} = 0$ and $K^y = 0$. The classical energies of the Hamiltonian with anisotropic terms (Eq. 2) in each spin configuration and direction of spin quantization axis are therefore given by:

$$\begin{pmatrix} E_{M||a}^{\text{FM}} \\ E_{M||b}^{\text{FM}} \\ E_{M||c}^{\text{FM}} \\ E_{M||a}^{\text{ferri}} \\ E_{M||b}^{\text{ferri}} \\ E_{M||c}^{\text{ferri}} \end{pmatrix} = \begin{pmatrix} 1 & 1 & 0 & 0 \\ 1 & 1 & 0 & 0 \\ 1 & 1 & nS^2 & nS^2 \\ 1 & 0 & 0 & 0 \\ 1 & 0 & 0 & 0 \\ 1 & 0 & -nS^2 & nS^2 \end{pmatrix} \begin{pmatrix} E_0 \\ \Delta_{\text{iso}}^{\text{FM}} \\ J_1^{zz} \\ K^z \end{pmatrix}. \quad (3)$$

Due to the crystal symmetry, the energies in a and b direction should be the same. In DFT estimates for the energies on the left-hand side, small deviations may occur due to imperfect convergence.

In the high-pressure monoclinic phase, the a and b directions are not equivalent any more. Therefore, finite anisotropy parameters in the y direction occur. The system of equations in the monoclinic phase reads:

$$\begin{pmatrix} E_{M||a}^{\text{FM}} \\ E_{M||b}^{\text{FM}} \\ E_{M||c}^{\text{FM}} \\ E_{M||a}^{\text{ferri}} \\ E_{M||b}^{\text{ferri}} \\ E_{M||c}^{\text{ferri}} \end{pmatrix} = \begin{pmatrix} 1 & 1 & 0 & 0 & 0 & 0 \\ 1 & 1 & nS^2 & 0 & nS^2 & 0 \\ 1 & 1 & 0 & nS^2 & 0 & nS^2 \\ 1 & 0 & 0 & 0 & 0 & 0 \\ 1 & 0 & -nS^2 & 0 & nS^2 & 0 \\ 1 & 0 & 0 & -nS^2 & 0 & nS^2 \end{pmatrix} \begin{pmatrix} E_0 \\ \Delta_{\text{iso}}^{\text{FM}} \\ J_1^{yy} \\ J_1^{zz} \\ K^y \\ K^z \end{pmatrix}. \quad (4)$$

We use Eq. 4 in both the trigonal and monoclinic phase and solve for the unknown parameters on the right-hand side using ordinary least squares. This also allows us to check the quality of our DFT energies, since perfect convergence should provide zero anisotropies in the trigonal phase for J_1^{yy} and K^y . Fig. 3(c) shows that we recover the zero values for J_1^{yy} and K^y almost perfectly.

B. Classical Monte Carlo

We performed classical Monte Carlo (cMC) simulations using the Metropolis-Hastings algorithm with local updates for $\text{Mn}_3\text{Si}_2\text{Te}_6$ as a function of pressure. We use a supercell of size $8 \times 8 \times 8$ with 3072 Mn sites in total. For each simulation we perform 5000 lattice sweeps for the warmup. Subsequently we perform 3000 measurements with 20 lattice sweeps for each. Each cMC run is averaged over the measurements of 512 parallel threads. Therefore, we perform $3072 \cdot (5000 + 3000 \cdot 20) \cdot 512 \approx 10^{11}$ Metropolis steps for each cMC result.

The exchange couplings illustrated in Fig. 2 were used to calculate and plot the specific heat, magnetic susceptibility and ordering temperatures. At ambient pressure, we find a peak in specific heat at 65 K (see Ref. [25]). Upon investigating the equilibrium spin configurations from our cMC data, we constructed polar plots of the spins in the ensemble. This allowed us to confirm that the ground state is ferrimagnetic, and the peak in specific heat corresponds to the ferrimagnetic transition temperature (T_C) [25]. We observe a nearly linear increase in T_C as a function of pressure in the trigonal phase. In the monoclinic phase, we anticipate a consequent nearly linear decrease in T_C based on experimental observations, which is indeed reflected in our Monte Carlo calculations in this phase. Hence, we successfully reproduced the dome-shaped behaviour in T_C as a function of pressure through our T_C simulations.

C. Anomalous Hall conductivity

Based on the full-relativistic DFT electronic structure, we estimate the intrinsic component of the anomalous Hall effect. The anomalous Hall conductivity σ_{xy} is defined as the integral of the total Berry curvature $\Omega_z(\vec{k})$ over the entire Brillouin zone (BZ) [36]:

$$\sigma_{xy} = -\frac{e^2}{\hbar} \int_{\text{BZ}} \frac{d\vec{k}}{(2\pi)^3} \Omega_z(\vec{k}) \quad (5)$$

The total Berry curvature $\Omega_z(\vec{k})$, calculated using Wannier interpolation within FPLO [37], is defined as the sum over all bands n of the band-resolved Berry curvature $\Omega_{n,z}(\vec{k})$ weighted by the respective occupation number $f_n(\vec{k})$ [36]:

$$\Omega_z(\vec{k}) = \sum_n f_n(\vec{k}) \Omega_{n,z}(\vec{k}) \quad (6)$$

As in our previous study for the similar van der Waals (vdW) ferromagnet CrGeTe_3 [30], we calculated the integral over the Brillouin zone in Eq. (5) using the **vegas** adaptive Monte Carlo algorithm [38, 39].

For each calculation of the anomalous Hall conductivity σ_{xy} we performed ten independent Monte Carlo runs with 10^6 evaluations of the integrand for training the adaptive part of the algorithm and subsequent 10^6 evaluations for the actual calculation of the conductivity. The ten independent runs allow us to estimate the standard deviation of the obtained results, i.e. the Monte Carlo uncertainty.

ACKNOWLEDGMENTS

We are grateful to Resta A. Susilo for help with the experimental crystal structures. H.O.J. acknowledges support through JSPS KAKENHI Grants No. 24H01668 and No. 25K0846007. Part of the computation in this work has been done using the facilities of the Supercomputer Center, the Institute for Solid State Physics, the University of Tokyo. The authors gratefully acknowledge the computing time provided on the supercomputers Lise and Emmy at NHR@ZIB and NHR@Göttingen as part of the German NHR infrastructure.

-
- [1] K. Manna, Y. Sun, L. Muechler, J. Kübler, and C. Felser, Heusler, Weyl and Berry, *Nat. Rev. Mater.* **3**, 244 (2018).
 - [2] Y. Tokura, K. Yasuda, and A. Tsukazaki, Magnetic topological insulators, *Nat. Rev. Phys.* **1**, 126 (2019).
 - [3] N. Nagaosa, T. Morimoto, and Y. Tokura, Transport, magnetic and optical properties of Weyl materials, *Nat. Rev. Mater.* **5**, 621 (2020).
 - [4] S. Nakatsuji and R. Arita, Topological magnets: Functions based on Berry phase and multipoles, *Annu. Rev. Condens. Matter Phys.* **13**, 119 (2022).
 - [5] B. A. Bernevig, C. Felser, and H. Beidenkopf, Progress and prospects in magnetic topological materials, *Nature* **603**, 41 (2022).
 - [6] E. Liu, Y. Sun, N. Kumar, L. Muechler, A. Sun, L. Jiao, S.-Y. Yang, D. Liu, A. Liang, Q. Xu, J. Kroder, V. Süß, H. Borrmann, C. Shekhar, Z. Wang, C. Xi, W. Wang, W. Schnelle, S. Wirth, Y. Chen, S. T. B. Goennenwein, and C. Felser, Giant anomalous Hall effect in a ferromagnetic kagome-lattice semimetal, *Nat. Phys.* **14**, 1125 (2018).
 - [7] Q. Wang, Y. Xu, R. Lou, Z. Liu, M. Li, Y. Huang, D. Shen, H. Weng, S. Wang, and H. Lei, Large intrinsic anomalous Hall effect in half-metallic ferromagnet $\text{Co}_3\text{Sn}_2\text{S}_2$ with magnetic Weyl fermions, *Nat. Commun.* **9**, 3681 (2018).
 - [8] K. Kim, J. Seo, E. Lee, K.-T. Ko, B. S. Kim, B. G. Jang, J. M. Ok, J. Lee, Y. J. Jo, W. Kang, J. H. Shim, C. Kim, H. W. Yeom, B. Il Min, B.-J. Yang, and J. S. Kim, Large

- anomalous Hall current induced by topological nodal lines in a ferromagnetic van der Waals semimetal, *Nat. Mater.* **17**, 794 (2018).
- [9] M. N. Ali, L. M. Schoop, C. Garg, J. M. Lippmann, E. Lara, B. Lotsch, and S. S. P. Parkin, Butterfly magnetoresistance, quasi-2D Dirac Fermi surface and topological phase transition in ZrSiS, *Sci. Adv.* **2**, e1601742 (2016).
- [10] T. Suzuki, L. Savary, J.-P. Liu, J. W. Lynn, L. Balents, and J. G. Checkelsky, Singular angular magnetoresistance in a magnetic nodal semimetal, *Science* **365**, 377 (2019).
- [11] E. Hassinger and T. Meng, Magnetic modification of electrical resistance, *Science* **365**, 324 (2019).
- [12] J. Seo, C. De, H. Ha, J. E. Lee, S. Park, J. Park, Y. Skourski, E. S. Choi, B. Kim, G. Y. Cho, H. W. Yeom, S.-W. Cheong, J. H. Kim, B.-J. Yang, K. Kim, and J. S. Kim, Colossal angular magnetoresistance in ferrimagnetic nodal-line semiconductors, *Nature* **599**, 576 (2021).
- [13] A. Das and S. Mukhopadhyay, Tuning the chiral orbital currents in a colossal magnetoresistive nodal-line ferrimagnet, *Phys. Rev. B* **111**, 174419 (2025).
- [14] Y. Ni, H. Zhao, Y. Zhang, B. Hu, I. Kimchi, and G. Cao, Colossal magnetoresistance via avoiding fully polarized magnetization in the ferrimagnetic insulator $\text{Mn}_3\text{Si}_2\text{Te}_6$, *Phys. Rev. B* **103**, L161105 (2021).
- [15] Y. Zhang, Y. Ni, H. Zhao, S. Hakani, F. Ye, L. DeLong, I. Kimchi, and G. Cao, Control of chiral orbital currents in a colossal magnetoresistance material, *Nature* **611**, 467 (2022).
- [16] H. Vincent, D. Leroux, D. Bijaoui, R. Rimet, and C. Schlenker, Crystal structure of $\text{Mn}_3\text{Si}_2\text{Te}_6$, *J. Solid State Chem.* **63**, 349 (1986).
- [17] A. F. May, Y. Liu, S. Calder, D. S. Parker, T. Pandey, E. Cakmak, H. Cao, J. Yan, and M. A. McGuire, Magnetic order and interactions in ferrimagnetic $\text{Mn}_3\text{Si}_2\text{Te}_6$, *Phys. Rev. B* **95**, 174440 (2017).
- [18] Y. Liu and C. Petrovic, Critical behavior and magnetocaloric effect in $\text{Mn}_3\text{Si}_2\text{Te}_6$, *Phys. Rev. B* **98**, 064423 (2018).
- [19] A. F. May, H. Cao, and S. Calder, Magnetic properties of ferrimagnetic $\text{Mn}_3\text{Si}_2\text{Te}_6$, *J. Magn. Magn. Mater.* **511**, 166936 (2020).
- [20] Y. Gu, K. A. Smith, A. Saha, C. De, C.-j. Won, Y. Zhang, L.-F. Lin, S.-W. Cheong, K. Haule, M. Ozerov, T. Birol, C. Homes, E. Dagotto, and J. L. Musfeldt, Unconventional insulator-to-metal phase transition in $\text{Mn}_3\text{Si}_2\text{Te}_6$, *Nat. Commun.* **15**, 8104 (2024).
- [21] Z. Zhang, G. Liu, W. Qi, H. Xie, J. Guo, Y. Du, T. Wang, H. Zhang, F. Zhou, J. Li, Y. Zhang, Y. Yu, F. Fei, X. Xi, and F. Song, Variation of magnetic properties with current in ferrimagnetic semiconductor $\text{Mn}_3\text{Si}_2\text{Te}_6$, *AIP Adv.* **14**, 035238 (2024).
- [22] R. A. Susilo, C. I. Kwon, Y. Lee, N. P. Salke, C. De, J. Seo, B. Kang, R. J. Hemley, P. Dalladay-Simpson, Z. Wang, D. Y. Kim, K. Kim, S.-W. Cheong, H. W. Yeom, K. H. Kim, and J. S. Kim, High-temperature concomitant metal-insulator and spin-reorientation transitions in a compressed nodal-line ferrimagnet $\text{Mn}_3\text{Si}_2\text{Te}_6$, *Nat. Commun.* **15**, 3998 (2024).
- [23] T. Mizokawa and A. Fujimori, Electronic structure and orbital ordering in perovskite-type 3d transition-metal oxides studied by Hartree-Fock band-structure calculations, *Phys. Rev. B* **54**, 5368 (1996).
- [24] Y. Iqbal, T. Müller, H. O. Jeschke, R. Thomale, and J. Reuther, Stability of the spiral spin liquid in MnSc_2S_4 , *Phys. Rev. B* **98**, 064427 (2018).
- [25] See Supplemental Material at [TO BE INSERTED BY THE EDITORS] for additional information on crystal structure prediction and calculation of specific heat using classical Monte Carlo simulations.
- [26] H.-X. Xu, M. Shimizu, D. Guterding, J. Otsuki, and H. O. Jeschke, Pressure evolution of electronic structure and magnetism in the layered van der Waals ferromagnet CrGeTe_3 , *Phys. Rev. B* **108**, 125142 (2023).
- [27] M. G. Gonzalez, V. Nocolak, A. Sharma, V. Favre, J.-R. Soh, A. Magrez, R. Bewley, H. O. Jeschke, J. Reuther, H. M. Rønnow, Y. Iqbal, and I. Živković, Dynamics of $\text{K}_2\text{Ni}_2(\text{SO}_4)_3$ governed by proximity to a 3D spin liquid model, *Nat. Commun.* **15**, 7191 (2024).
- [28] L. D. C. Jaubert, Y. Iqbal, and H. O. Jeschke, Spin-peierls transition in the frustrated spinels ZnCr_2O_4 and MgCr_2O_4 , *Phys. Rev. Lett.* **134**, 086702 (2025).
- [29] J. Ebad-Allah, D. Guterding, M. Varma, M. Diware, S. Ganorkar, H. O. Jeschke, and C. A. Kuntscher, Near room-temperature ferromagnetism from double exchange in the van der Waals material CrGeTe_3 : Evidence from optical conductivity under pressure, *Phys. Rev. B* **111**, L140402 (2025).
- [30] G. Scharf, D. Guterding, B. Hen, P. M. Sarte, B. R. Ortiz, G. K. Rozenberg, T. Holder, S. D. Wilson, H. O. Jeschke, and A. Ron, Pressure tuning of intrinsic and extrinsic sources to the anomalous Hall effect in CrGeTe_3 , *Phys. Rev. Res.* **7**, 013127 (2025).
- [31] G. Scharf, A. N. Gaon, P. M. Sarte, B. R. Ortiz, S. D. Wilson, and A. Ron, Light-induced ferromagnetism above the Curie temperature in CrGeTe_3 , *Phys. Rev. B* **111**, L100408 (2025).
- [32] S. Zhang, K. Harii, T. Yokouchi, S. Okayasu, and Y. Shiomi, Amorphous ferromagnetic metal in van der Waals materials, *Adv. Electron. Mater.* **10**, 2300609 (2024).
- [33] K. Koepnick and H. Eschrig, Full-potential nonorthogonal local-orbital minimum-basis band-structure scheme, *Phys. Rev. B* **59**, 1743 (1999).
- [34] J. P. Perdew, K. Burke, and M. Ernzerhof, Generalized gradient approximation made simple, *Phys. Rev. Lett.* **77**, 3865 (1996).
- [35] A. I. Liechtenstein, V. I. Anisimov, and J. Zaanen, Density-functional theory and strong interactions: Orbital ordering in Mott-Hubbard insulators, *Phys. Rev. B* **52**, R5467 (1995).
- [36] X. Wang, J. R. Yates, I. Souza, and D. Vanderbilt, Ab initio calculation of the anomalous Hall conductivity by Wannier interpolation, *Phys. Rev. B* **74**, 195118 (2006).
- [37] H. Eschrig and K. Koepnick, Tight-binding models for the iron-based superconductors, *Phys. Rev. B* **80**, 104503 (2009).
- [38] G. P. Lepage, A new algorithm for adaptive multidimensional integration, *J. Comput. Phys.* **27**, 192 (1978).
- [39] G. P. Lepage, Adaptive multidimensional integration: vegas enhanced, *J. Comput. Phys.* **439**, 110386 (2021).

Origin of pressure-induced anomalies in the nodal-line ferrimagnet $\text{Mn}_3\text{Si}_2\text{Te}_6$ – Supplemental Material –

Varun Venkatasubramanian,¹ Makoto Shimizu,² Daniel Guterding,³ and Harald O. Jeschke¹

¹Research Institute for Interdisciplinary Science, Okayama University, Okayama 700-8530, Japan

²Department of Physics, Graduate School of Science, Kyoto University, Kyoto 606-8502, Japan

³Technische Hochschule Brandenburg, Magdeburger Straße 50, 14770 Brandenburg an der Havel, Germany

I. ADDITIONAL DFT RESULTS

In Figs. S1 and S2, we present the structural information that is the basis for all further calculations. Lattice parameters as function of pressure are taken from experiment and interpolated. For the trigonal $P\bar{3}1c$ phase, internal coordinates are optimized with a generic DFT+U functional in the ferromagnetic state. Relaxation in ferrimagnetic state yields very similar results.

For the monoclinic structure, we find that structure relaxation takes the internal coordinates too far away from the experimentally determined ones. Therefore, we only vary the lattice parameters as shown in Fig. S2 and keep the internal coordinates fixed at the values of the $P = 22.3$ GPa experimental structure. The corresponding bond lengths are shown in Fig. S3.

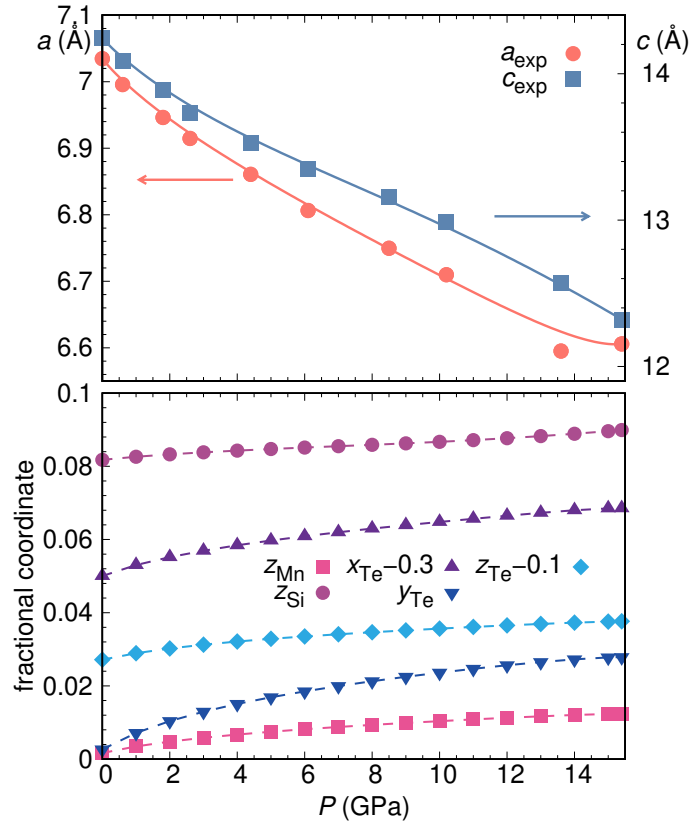


FIG. S1. Structure parameters of $\text{Mn}_3\text{Si}_2\text{Te}_6$ as a function of pressure for the $P\bar{3}1c$ space group. (a) Interpolated lattice parameters; symbols are experimental points taken from Ref. 1. Lines are smooth interpolations that were used for this study. (b) Fractional coordinates of $\text{Mn}_3\text{Si}_2\text{Te}_6$ determined by relaxation of the structures with a DFT+U functional at $U = 5$ eV in a ferromagnetic state. Dashed lines are guides to the eye.

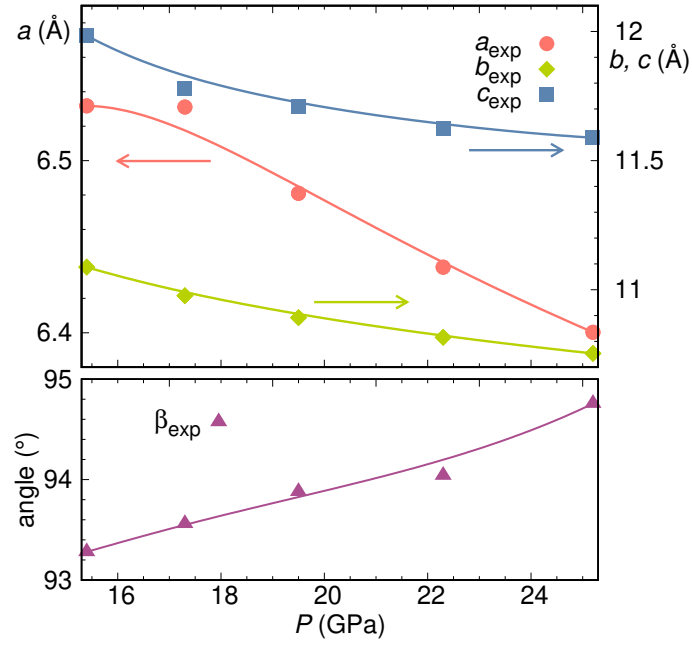


FIG. S2. Structure parameters of $\text{Mn}_3\text{Si}_2\text{Te}_6$ as a function of pressure for the $C2/c$ space group. (a) Interpolated lattice parameters and (b) monoclinic β angle; symbols are experimental points taken from Ref. 1. Lines are smooth interpolations that were used for this study.

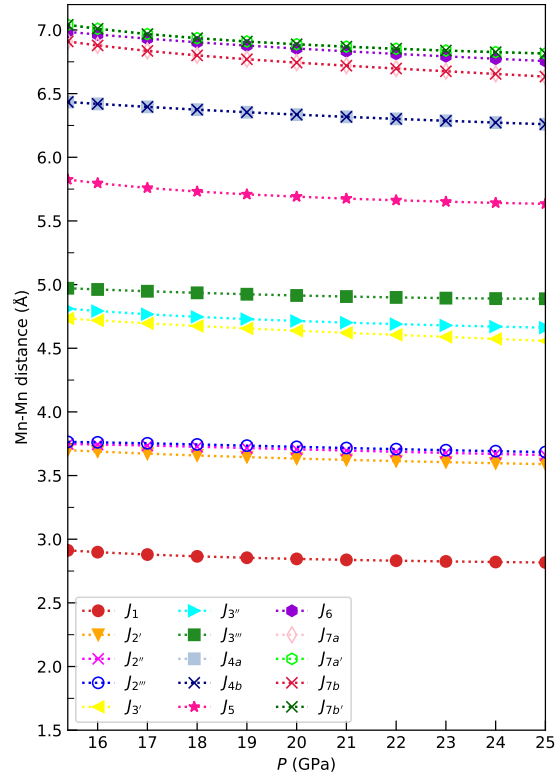


FIG. S3. Evolution of the nearest neighbour Mn-Mn distances as a function of pressure for the monoclinic structures of $\text{Mn}_3\text{Si}_2\text{Te}_6$.

II. ADDITIONAL MONTE CARLO RESULTS

We present the calculated specific heat for trigonal and monoclinic structures of $\text{Mn}_3\text{Si}_2\text{Te}_6$ in Figures S4 and S5. We use the position of the maxima to determine the ferrimagnetic ordering temperatures plotted in Fig. 4 of the main text.

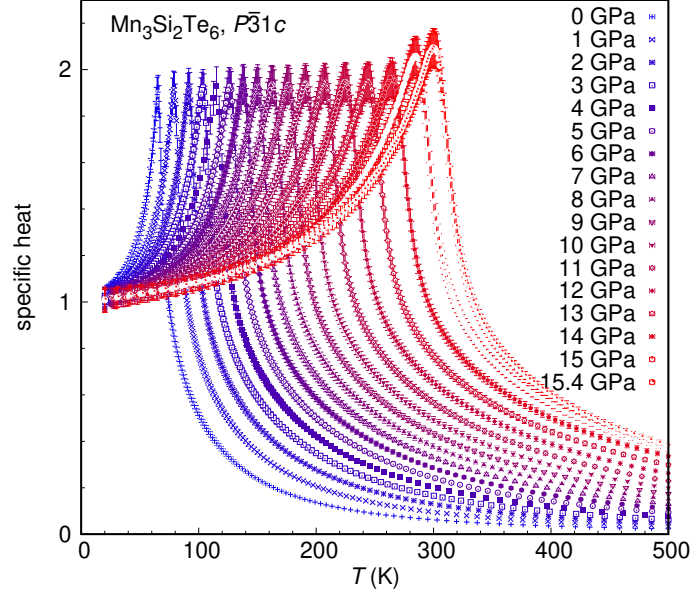


FIG. S4. Specific heat for the trigonal $P\bar{3}1c$ structure of $\text{Mn}_3\text{Si}_2\text{Te}_6$. Pressures range from $P = 0$ to $P = 15.4$ GPa.

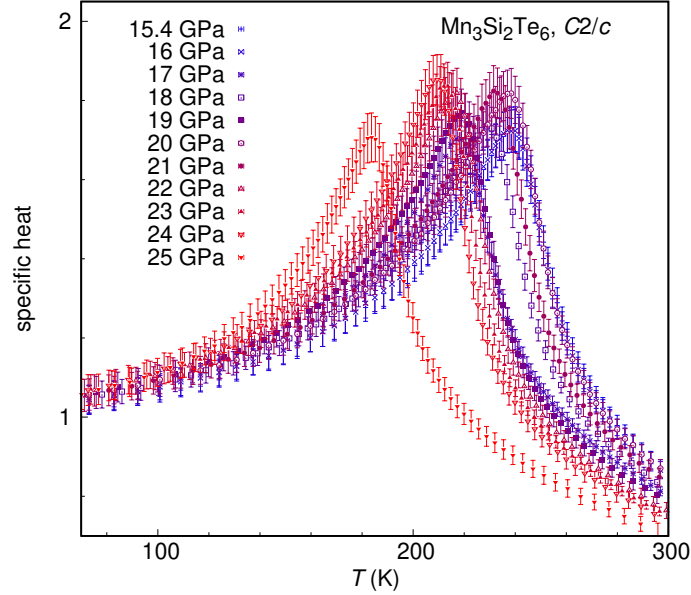


FIG. S5. Specific heat for the monoclinic $C2/c$ structure of $\text{Mn}_3\text{Si}_2\text{Te}_6$. Pressures range from $P = 15.4$ GPa to $P = 25$ GPa.

We also present, in Figures S6 and S7, the magnetization curves as function of temperature for all pressure values we considered. The magnetization value $1/3$ corresponds to the ferrimagnetic state where Mn trimers are in an up-down-up state and all trimers in the lattice are ferromagnetically ordered. In the monoclinic phase, some frustration in the Hamiltonian leads to a small modulation of the ferrimagnetic state so that the total magnetization for example for 15.4, 16 and 17 GPa does not reach the full $1/3$.

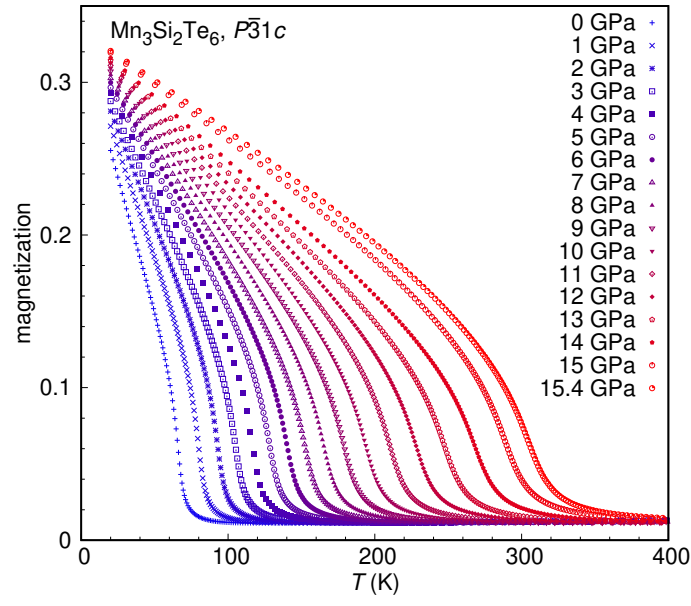


FIG. S6. Absolute value of the unit cell magnetization for the $P\bar{3}1c$ structure of $\text{Mn}_3\text{Si}_2\text{Te}_6$. Pressures range from $P = 0$ to $P = 15.4$ GPa. The value $1/3$ corresponds to the ferrimagnetic state.

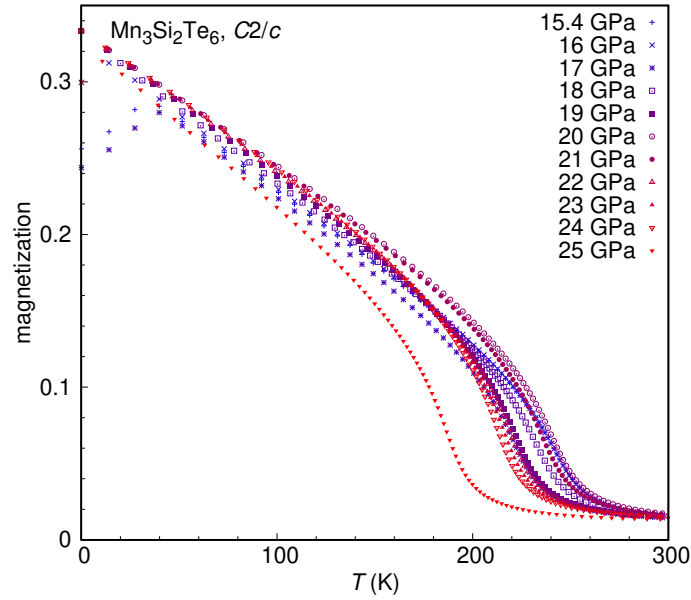


FIG. S7. Absolute value of the unit cell magnetization for the $C2/c$ structure of $\text{Mn}_3\text{Si}_2\text{Te}_6$. Pressures range from $P = 15.4$ GPa to $P = 25$ GPa. The value $1/3$ corresponds to the ferrimagnetic state.

-
- [1] R. A. Susilo, C. I. Kwon, Y. Lee, N. P. Salke, C. De, J. Seo, B. Kang, R. J. Hemley, P. Dalladay-Simpson, Z. Wang, D. Y. Kim, K. Kim, S.-W. Cheong, H. W. Yeom, K. H. Kim, and J. S. Kim, High-temperature concomitant metal-insulator and spin-reorientation transitions in a compressed nodal-line ferrimagnet $\text{Mn}_3\text{Si}_2\text{Te}_6$, [Nat. Commun. **15**, 3998 \(2024\)](#).